Extreme Mechanics Letters 60 (2023) 101983

Contents lists available at ScienceDirect

Extreme Mechanics Letters

journal homepage: www.elsevier.com/locate/eml

Parametric analysis of multi-material soft sensor structures for enhanced strain sensitivity

Myungsun Park, Taejun Park, Yong-Lae Park *

Department of Mechanical Engineering, Institute of Advanced Machines and Design, Institute of Engineering Research, Seoul National University, 1 Gwanak-ro, Gwanak-gu, Seoul 08826, Republic of Korea

A R T I C L E I N F O

Article history:
Received 25 August 2022
Received in revised form 7 February 2023
Accepted 20 February 2023
Available online 23 February 2023

Keywords:
Soft sensors
Soft robotics
Liquid metal
Sensitivity
Multi-material
Multi-stiffness

A B S T R A C T

Soft strain sensors that utilize geometrical changes of elastomer structures embedded with conductive liquid have advantage of physical compliance and dynamic durability. Approaches to enhancing their sensitivities are however limited, since the output resistance is dependent only on the single input, i.e., strain. In this paper, a multi-material strain sensor structure is proposed to overcome the limitation in improving the sensitivity. We define two design parameters that determine the strain sensitivity: the stiffness ratio and the length portion of the different materials used in the structure. Investigations on the effects of the parameters on the sensor performances, including the sensitivity, the stiffness, the resolution, the hysteresis, the linearity, the durability, and the maximum strain, are conducted by deriving a global mathematical model validated through experiments. Based on the results, there exists the optimal length portion of the component materials that maximizes the sensitivity, depending on the stiffness of each material component. We demonstrate an example, using the optimized parameters, of a multi-material sensor with the highest resolution three times that of a conventional single-material sensor. We also demonstrate that the high precision achieved in the proposed multi-material sensor structure enables successful measurement of the tiny movements of a human finger. Lastly, potential design improvements are provided so that the structure can further enhance its structural integrity and compliance.

1. Introduction

Highly stretchable strain sensors [1–3] have been widely used for measuring motions of various systems with large deformation, including human bodies and soft robots. They not only provide high conformity to irregular surfaces but also hardly induce physical interference to the movements of the host systems. Research in improving the performances of soft strain sensors, such as sensitivity, stretchability, hysteresis, linearity, and durability [4,5], have been reported through different approaches [6].

Amjadi et al. [4] categorized the stretchable strain sensors into five types according to their sensing mechanisms: geometrical effect, piezoresistive effect, disconnection, crack propagation, and tunneling effect. Among these mechanisms, the geometrical effect utilizes the change in the cross-sectional area of the sensor's conductive path when stretched. If conductive liquid, such as room-temperature liquid metal [7,8] or ionic liquid [9], is used as a sensing medium filling the microchannels embedded in an elastomer structure, its inherent conformity allows the sensor to attain superior stretchability and dynamic durability to other sensing mechanisms [10–12]. Therefore, a wide range of applications including skin-like electronics [13], wearable devices [14–16], human–robot interactions [17,18], sensorized soft robots [19–23], and even commercialized sensing systems [24], have been developed based on the geometrical effect.

A high sensitivity in strain sensing is especially critical to some of these applications. For example, sensors for detecting human finger movements [13,25], ranging from small tremors to large flexion and extension motions, need to provide a high resolution while covering a large range of deformation. Previous studies [26,27] argues that hand tracking systems are required to have a resolution as high as 0.2 mm for detecting the displacement at the fingertip, considering the tremor of healthy young people [28,29].

However, progress in enhancing the sensitivity has been limited by the physical property of the sensing medium in geometry-based strain sensors. The resistance change of the conductive liquid channel (or trace) can be modeled as a function of the length of the path, L, the cross-sectional area, A, and the resistivity, ρ, from the well known equation $R = \rho L/A$. Assuming the incompressibility of liquid and the constant resistivity under deformation, the equation can be rewritten in terms of strain,

* Corresponding author.
E-mail addresses: arielrbts@snu.ac.kr (M. Park), taejunpark@snu.ac.kr (T. Park), ylpark@snu.ac.kr (Y.-L. Park).

https://doi.org/10.1016/j.eml.2023.101983
2352-4316/

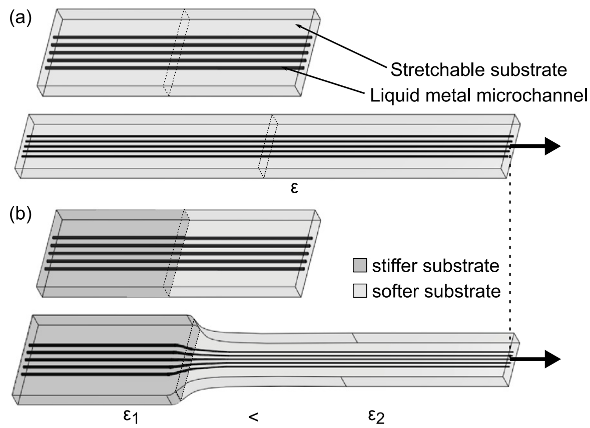

Fig. 1. Comparison of single-material and multi-material sensors: (a) Deformation of a single-material sensor due to uniaxial tension, which produces uniform strain across the sensor; (b) Deformation of a multi-material sensor due to uniaxial tension. Each segment experiences distinct strains.

ϵ, [4,5,30,31] as

$$\frac{\Delta R}{R_0} = \frac{\Delta(L/A)}{L_0/A_0} = 2\epsilon + \epsilon^2. \tag{1}$$

Eq. (1) shows that strain, the input of the system, is the only factor that determines the change of the sensor's resistance, and the sensitivity cannot be controlled by changing the geometrical parameters, such as the area or the length of the conductive channel.

We previously suggested an approach to enhancing the sensitivity by modulating the strain distribution of the sensor given the same input, introducing a multi-material sensor structure [32]. Unlike conventional sensors made of a single material (Fig. 1(a)), each material segment embedded with a conductive path in the multi-material structure (Fig. 1(b)) experiences a distinct strain. More specifically, the soft segment experiences a larger strain than the stiff segment. The total resistance change of the sensor is then calculated as the sum of the local resistance changes of all the segments. This work was successful in demonstrating the advantage of multi-material structures through experiments. However, it did not provide a theoretical analysis that explains the principle of the sensitivity enhancement based on relevant design parameters. In addition, the experimental observations were conducted in a limited scope—only a single pair of materials were used to create the multi-material structures of the prototypes that covered only a few different length portions of the composing materials.

In this study, we present a thorough analysis on the multi-material sensors and provide a guidance to their effective implementation to practical applications. We first investigate the mechanisms through which the multi-material structures enhance the sensitivity. By introducing two key design parameters, the stiffness ratio and the length portion of the component materials, we provide a closed-form solution that explains the behavior of each component and the resultant resistance of the sensor. The suggested model is global, covering the entire range of the parameters, and enables optimization of the design that enhances the sensitivity. The global parametric effects and the optimality from the model are then experimentally validated using actual sensor prototypes. Considering the nonlinear characteristics of the composing materials, the model is further elaborated to describe the behavior of the multi-material sensors. Finally, we highlight the significance of the sensitivity enhancement by measuring the small tremor of the human hand with an exceptional resolution of 10 μm that is impossible to achieve using conventional single-material soft sensors. We also suggest possible design variations to further improve the structural robustness and softness of the multi-material sensors.

The rest of the paper is organized as follows. In Section 2, we formulate the closed-form expressions of the sensitivity of multi-material soft sensors following the introduction of their design parameters. Section 3 describes the fabrication process and the testing procedure of the sensor prototypes for validation of the proposed model. Section 4 compares the experimental results with the theoretical predictions. The sensors are further evaluated with regard to other performance criteria, including the minimum resolution, the hysteresis, the linearity, the dynamic durability, and the maximum strain. Based on the results, the optimal parameters of a multi-material sensor are derived for measuring human finger motions in Section 5. Experiments with the corresponding sensor prototype are then conducted to demonstrate the effectiveness of the enhanced sensitivity. Section 6 finally discusses several design improvements for the shortcomings of the multi-material structure.

2. Theory

2.1. Introduction of two design parameters

To maximize the sensitivity and to optimize the design for required specifications, we define two design parameters of a multi-material sensor structure. The local resistance change along the sensing (i.e., conductive) path is determined by the corresponding local strains according to Eq. (1). The modulation of these local strains (i.e., the distinct strains in different material segments) in the multi-material structure can be achieved by altering the stiffness variation and the length portion of the elastomer materials. To investigate how these factors affect the strain distribution, deformations of multi-material structures with varying material combinations (Fig. 2(a)) and length portions (Fig. 2(b)) were simulated using a commercialized finite element analysis software package (Abaqus, Dassault Systems).

In the simulation results, shown in Fig. 2, the strain contours of the deformed structure and the strain distributions along the length of the sensors are shown. In all designs, we observed that the strain applied to each material segment was almost uniform, which allowed us to model the multi-material sensor with an assumption of piece-wise constant strains over the length of the sensor. By comparing the three sensors shown in Fig. 2(a), we found that the larger differences in the stiffness of the materials lead to the greater differences in the strain levels between the two segments. More specifically, the differences in the strain levels decreased from approximately 1.58 to 0.64 and ended up approaching 0 as the difference in the stiffnesses of the two materials became smaller, as shown in Fig. 2(a) i–iii. Increasing the portion of the stiffer material increased the strains in both material segments, as shown in Fig. 2(b), leading to an increase in the total resistance based on Eq. (1).

2.2. Two-parameter analysis

2.2.1. Governing equations and solution

For multi-material sensors, we assume that the geometry of the embedded conductive path is uniform in the undeformed state, regardless of the component materials. With a uniform cross-sectional area, the initial resistance of each material segment is determined only by its initial length. We then establish the total resistance of the multi-material sensor as the sum of the

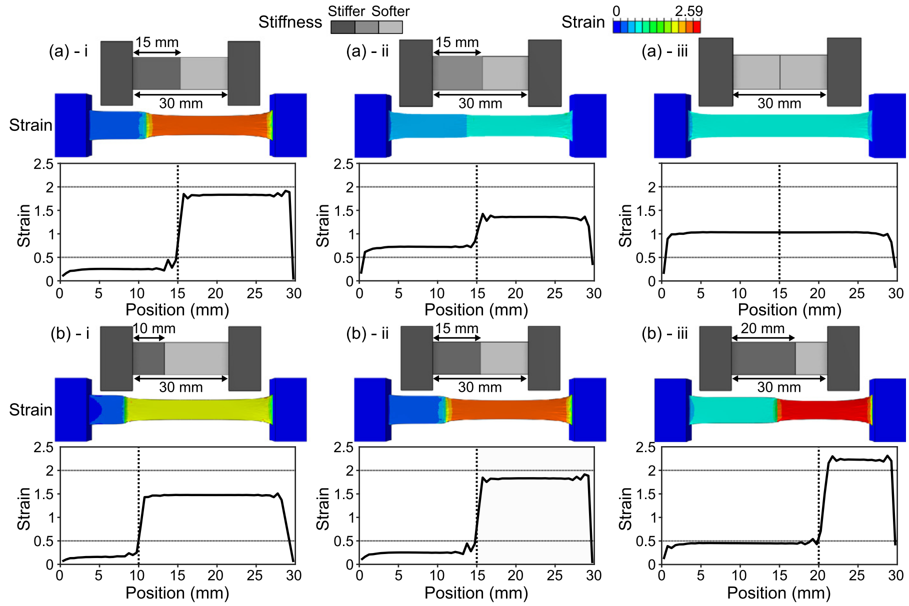

Fig. 2. Deformation of multi-material sensors with design variations predicted by finite element analysis. Strains (*y*-axis) along the length of the sensor (*x*-axis) are plotted: (a) Sensors with various material combinations; the difference in the stiffnesses of the composing materials decreases from left to right. (b) Sensors with different length portions of a stiffer material (33%, 50%, 66%).

local resistances, each of which was calculated using Eq. (1). Thus,

$$\begin{aligned}\frac{\Delta R}{R_0} &= \frac{R_{1,0}(2\epsilon_1+\epsilon_1^2)+R_{2,0}(2\epsilon_2+\epsilon_2^2)}{R_{1,0}+R_{2,0}} \\ &= \frac{R_{1,0}}{R_{1,0}+R_{2,0}}(2\epsilon_1+\epsilon_1^2)+\frac{R_{2,0}}{R_{1,0}+R_{2,0}}(2\epsilon_2+\epsilon_2^2) \\ &= \frac{l_{1,0}}{l_{1,0}+l_{2,0}}(2\epsilon_1+\epsilon_1^2)+\frac{l_{2,0}}{l_{1,0}+l_{2,0}}(2\epsilon_2+\epsilon_2^2)\end{aligned} \tag{2}$$

where the subscript 0 in the variables indicates the initial value before the sensor deformation, and the subscripts 1 and 2 represent the types of the materials in the different segments. Now, the total resistance change of a multi-material sensor can be expressed with second-order polynomials of the local strains as well as with the initial lengths of the segments. The local strains can be calculated by solving the geometric constraints and the force equilibrium of the sensor. The total strain (ϵ) of the sensor is geometrically related to the local strains by

$$l_{1,0}\epsilon_1 + l_{2,0}\epsilon_2 = (l_{1,0}+l_{2,0})\epsilon. \tag{3}$$

Then, the tensile force equilibrium of the material segments connected in series needs to be satisfied. We first consider a simple case in which the materials follow the linear force–strain relation as

$$K_1\epsilon_1 = K_2\epsilon_2, \tag{4}$$

where K_1 and K_2 are the stiffnesses of the two materials. K_1, K_2, $l_{1,0}$, and $l_{2,0}$, used to express the constraining equations (Eqs. (3) and (4)), can be further simplified to two parameters as

$$\begin{aligned}s &:= K_1/K_2 \in \mathbb{R}, \\ l &:= l_{1,0}/(l_{1,0}+l_{2,0}) \in \mathbb{R},\end{aligned} \tag{5}$$

by setting K_1 to be larger than K_2 without loss of generality. We denote s as the stiffness ratio between the two materials and l as the length portion of the stiffer material. A sensor with $l = 0$ or $l = 1$ indicates a sensor made of a single material to be entirely soft or stiff, respectively. If the sensor has a large s, the two materials forming the multi-material structure have a large difference in stiffness. Now, Eqs. (3) and (4) can be solved, and the local strains of the two material segments (ϵ_1, ϵ_2) can be expressed using the two parameters (s, l) and the total strain (ϵ) as

$$\epsilon_1 = \frac{\epsilon}{s+l-sl}, \tag{6a}$$

$$\epsilon_2 = \frac{s\epsilon}{s+l-sl}. \tag{6b}$$

By plugging these local strains into Eq. (2), we can finally derive the total resistance change of a multi-material sensor in a closed form as

$$\begin{aligned}\frac{\Delta R}{R_0} =& l\left(\frac{2\epsilon}{s+l-sl}+\frac{\epsilon^2}{(s+l-sl)^2}\right) \\ &+ (1-l)\left(\frac{2s\epsilon}{s+l-sl}+\frac{s^2\epsilon^2}{(s+l-sl)^2}\right).\end{aligned} \tag{7}$$

2.2.2. Analysis

To understand the effects of the parameters s and l in Eq. (7), the equation was plotted in Fig. 3 for a fixed input strain (ϵ) of 1 (100% of stretching from the initial length). Each curve represents a different material combination, showing the resistance change as the length portion varies. The flat curve ($s = 1$, black) is a single-material sensor, which is not affected by the changes of the length portion. However, for a large stiffness ratio with distinct materials forming the sensor, we see that the multi-material structure shows greater changes in resistance than does the single-material structure. We also note that the resistance change does not monotonically increase with the increase of the length portion, but rather, a peak exists in each curve (marked with an asterisk). This observation signifies the existence of the optimal length portion for each stiffness ratio. These optimal points can be computed by differentiating Eq. (7). Given the stiffness ratio, the optimal resistance change ($\Delta R/{R_0}^*$) and the corresponding length portion (l^*) are calculated as

$$\left(\frac{\Delta R}{R_0}\right)^*(s,\epsilon) = \frac{\epsilon(\epsilon+8s+2\epsilon s+\epsilon s^2)}{4s} \tag{8a}$$

$$l^*(s) = \frac{s}{1+s}. \tag{8b}$$

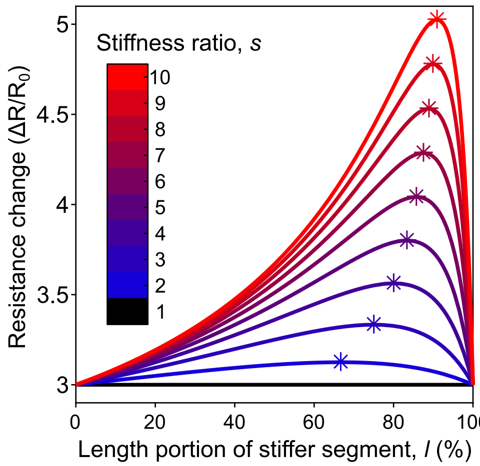

Fig. 3. Resistance changes at 100% strain normalized by the initial resistances ($\Delta R/R_0$), i.e., sensitivity, for varied length portions of the stiffer segment and the stiffness ratios.

Lastly, we observed that the overall curve shifted upwards, and the peak rightwards, as the stiffness ratio (s) increased. Therefore, to enhance the sensitivity of a multi-material strain sensor, it is ideal to select materials with a stiffness difference as large as possible with the optimal length portion.

3. Experiments

To evaluate the validity of the model, presented in Section 2, which describes the sensitivity of multi-material sensors, sensor prototypes with various design parameters were fabricated and tested to examine their behaviors. Each of these fabricated sensors was also modeled based on the theory, discussed in Section 2, combined with an elaborate force–strain relation.

3.1. Sensor fabrication and testing

3.1.1. Sensor design

To investigate the effect of the stiffness ratio on the multi-material sensors, two different stiffness ratios (i.e. two different combinations of silicone materials) were used: a combination of Ecoflex 00-30 (100% modulus: 69 kPa, Smooth-on, Inc.) and Dragon Skin 30 (100% modulus: 593 kPa, Smooth-On, Inc.), and a combination of Ecoflex 00-30 and a 1:1 mixture (mass ratio) of Ecoflex 00-30 and Dragon Skin 30, which we will denote as Ecoflex–DragonSkin mixture. For each combination, sensor samples with seven different length portions were fabricated with the stiffer material occupying 0%, 33.3%, 50%, 66.7%, 83.3%, and 100% of the total length.

The dimensions and the fabrication process of the multi-material sensors are summarized in Fig. 4(a) and (b). Plastic molds were prepared by 3D-printing and assembled so that two different silicone materials could be cured one after the other. After preparation of all the molds, liquid-state Dragon Skin 30 was poured into the mold and cured. The remaining space was then filled with Ecoflex 00-30 and cured. Using a motorized x–y stage (Shotmaster 300ΩX, Musashi), a pneumatic dispensing system (SuperΣ CMIII V2, Musashi), and a laser distance sensor (LK-G32, Keyence), liquid-metal (eutectic gallium-indium, eGaIn) traces were printed on the top surface of the cured silicone. Reliable and efficient fabrication of eGaIn traces was achieved [33,34] by controlling the thickness of the liquid metal using the dispensing pressure, the stand-off distance, the stage velocity, and the shot time [35,36]. The printed eGaIn traces were then encapsulated by a thin layer of the Ecoflex–DragonSkin mixture. A block of Dragon Skin 30 was also cured on each end of the sensor as a holder combined with a custom-built fixture during testing. For fabrication of the samples with the other stiffness ratios, the entire procedure was repeated except for replacing the stiff material (Dragon Skin 30) with the Ecoflex–DragonSkin mixture.

3.1.2. Experimental setup

The resistance and the tensile force of the multi-material sensor samples were measured during uni-axial tensile tests. Each sensor was fixed on a motorized test stand (ESM 303, Mark-10) (Fig. 4(c)). The seven samples were tested for each length portion, and all the sensors were stretched up to 100% strain prior to the main experiment accounting for the Mullins effect [37,38].

For tests involving displacements smaller than 0.1 mm, a universal material testing machine (34C-1, Instron) was used with the same experiment.

3.2. Elaborated force–strain relation

There are limitations in directly applying Eq. (4) and consequently Eq. (7), in Section 2, to actual soft sensors for validation of the proposed model. We previously employed a simplified linear force–strain relationship in order to discuss the parameter of the stiffness ratio as a single variable s. In this way, we can

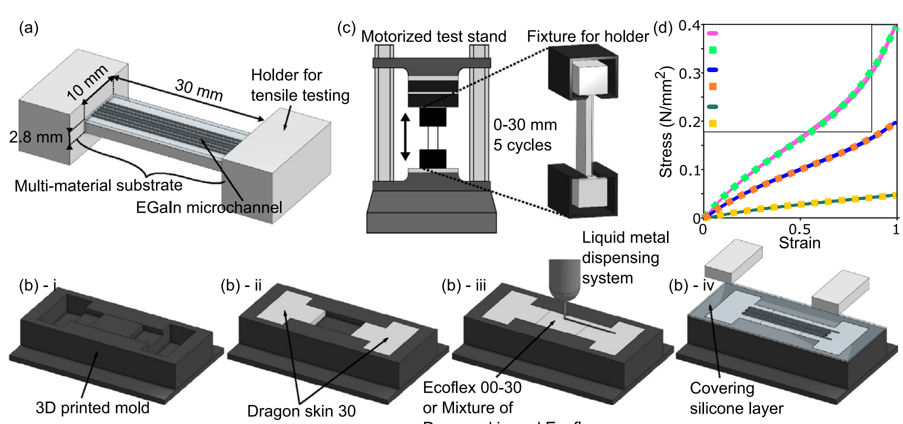

Fig. 4. Overview of sensor prototyping and testing: (a) design, (b) fabrication process of the multi-material sensor, (c) experimental setup for the cyclic tensile test, and (d) hyperelastic Yeoh model characterization of the materials used in the experiment. The solid and the dotted lines represent the measured and fitted stress data, respectively.

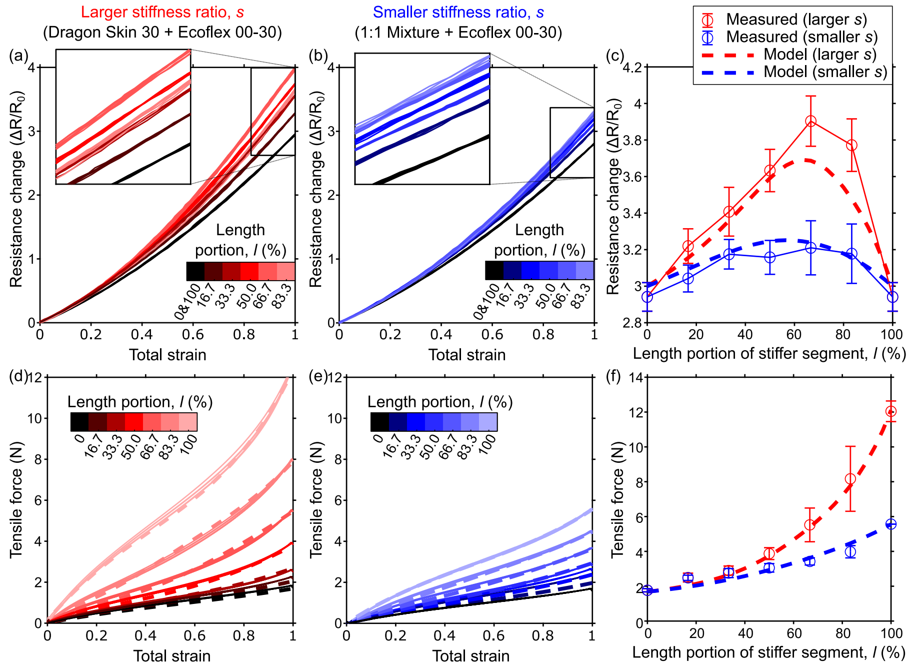

Fig. 5. Resistance changes and tensile forces of multi-material sensors with various design parameters. (a) Resistance curves of sensors with the high stiffness ratio (i.e., combination of Dragon Skin 30 and Ecoflex 00-30). (b) Resistance curves of sensors with the low stiffness ratio (i.e., combination of Ecoflex–DragonSkin mixture and Ecoflex 00-30). The shades of the color indicate different length portion, with the brighter shades representing larger portions of the stiff segment. (c) Model predictions (dotted lines) from Section 3.2 and measured resistance (circular markers) at 100% strain (data points at strain = 1 in (a) and (b)) plotted with respect to length portions. The length portions are expressed in x-axis. Error bars were calculated with seven samples of each sensor design. (d) Tensile force curves of sensors with the high stiffness ratio. (e) Tensile force curves of sensors with the low stiffness ratio. (f) Model predictions (dotted lines) from Section 3.2 and measured tensile forces (circular markers) at 100% strain (data points at strain = 1 in (a) and (b)) plotted with respect to length portions. (For interpretation of the references to color in this figure legend, the reader is referred to the web version of this article.)

obtain the intuition on the effects of the two parameters on the behavior of the multi-material sensors. However, the simplified relation does not reflect the true nature of silicone materials in general. Therefore, we adopted the hyperelastic Yeoh model into the theories in Section 2 for accurate prediction of the behavior of the tested samples instead of using the simplified relationship. The Yeoh model is considered to be suitable in interpreting the sensors made of silicone materials, since they experience local strains ranging from 0 to 300% during the tensile test [39,40].

The third-order Yeoh model suggests that the tensile force (F) can be expressed with the stretch λ ($= \epsilon + 1$) and the three material constants (C_1, C_2, C_3) as

$$F = 2\,A_0\left(\lambda - \frac{1}{\lambda^2}\right)\sum_{i=1}^{3} i\,C_i\left(\lambda^2 + \frac{2}{\lambda} - 3\right)^{i-1}. \tag{9}$$

Using this relation, the force equilibrium in Eq. (4) can be rewritten as

$$\begin{aligned} &2\left(\lambda_1 - \frac{1}{\lambda_1^2}\right)\left(C_{1,1} + 2C_{1,2}(I_1 - 3) + 3C_{1,3}(I_1 - 3)^2\right) \\ &= 2\left(\lambda_2 - \frac{1}{\lambda_2^2}\right)\left(C_{2,1} + 2C_{2,2}(I_2 - 3) + 3C_{2,3}(I_2 - 3)^2\right), \end{aligned} \tag{10}$$

where $\lambda_k = \epsilon_k + 1$, $I_k = \lambda_k^2 + 2/\lambda_k$, and $(C_{k,1}, C_{k,2}, C_{k,3})$ representing the three Yeoh coefficients of the kth material.

Then, given the Yeoh coefficients and the length portion l, the local strain of each segment in a multi-material structure is calculated by solving Eq. (10) with Eq. (3). The calculated local strains are then plugged into Eqs. (2) and (10) to quantify the sensitivity and the force associated with each sensor.

The force–strain curves of the three silicone materials used for fabrication (Ecoflex 00-30, Dragon Skin 30, and a 1:1 mixture of the two silicone) were fitted with Eq. (9) to obtain the corresponding Yeoh coefficients of the material (Fig. 4(d)). The plots show that the stiffness of the mixed material is approximately the average of the two pure materials. The calculations of the model and the experimental results will be discussed in detail in Section 4.

4. Results

Sensors with two different stiffness ratios (Dragon Skin 30 + Ecoflex 00-30 and Ecoflex–DragonSkin Mixture + Ecoflex 00-30) and seven different length portions (0%, 16.7%, 33.3%, 50%, 66.7%, 83.3%, 100%) were tested to confirm the effects of the two design parameters on the sensor performances.

4.1. Enhanced sensitivity of multi-material sensors and optimal length portion

Figs. 5(a) and 5(b) show the resistance changes of the sensors with seven different length portions. Fig. 5(a) shows the results from the sensors with higher stiffness ratios (Dragon Skin 30 + Ecoflex 00-30) than those in Fig. 5(b) (Ecoflex–DragonSkin Mixture + Ecoflex 00-30). The curves were plotted with respect to the total strain ranging from 0 to 1.

In both material combinations, i.e., Figs. 5(a) and 5(b), all the multi-material sensors (colored in red or blue) demonstrated higher resistance changes than the single-material sensors (black). However, the response curves varied among the sensors with different length portions. A more detailed comparison is depicted in Fig. 5(c) that marks each sensor's resistance change at a total strain of 100% ($\epsilon = 1$), equivalent to the gauge factor. Each marker represents the last data point of the curve in Figs. 5(a) and 5(b), plotted with respect to the length portion. The two solid line curves, connecting these markers, are both bell-shaped, with the minimum values at 0 and 100% length portion, representing

Table 1
Nonlinearity of sensors with various design parameters (Stiffness ratios and length portions). Nonlinearity were evaluated by the percentage of deviation (error) from the best fit line to the full scale output (FSO) of the sensor.

Stiffness ratio	High (Dragon Skin 30 + Ecoflex 00-30)						Low (Mixed material + Ecoflex 00-30)					
Length portion (%)	0 & 100	16.7	33.3	50.0	66.7	83.3	0 & 100	16.7	33.3	50.0	66.7	83.3
Nonlinearity (%FSO)	6.8	5.9	7.3	6.3	7.2	6.8	7.5	6.1	7.9	6.8	8.3	8.0

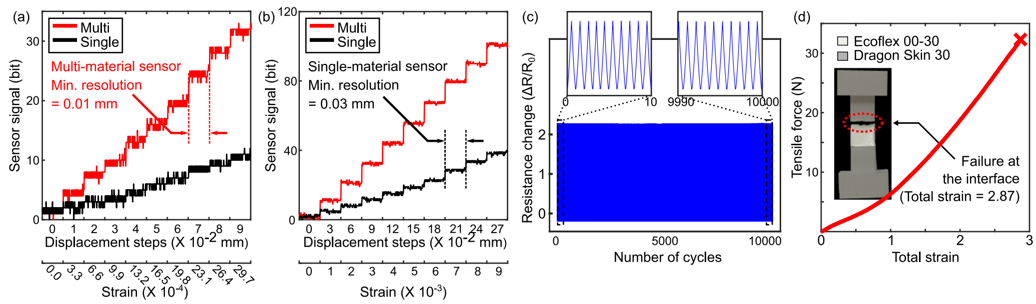

Fig. 6. Resolution and durability of the multi-material sensor. (a) Sensor signals (digital bits) of the multi-material sensor with the highest sensitivity, in Fig. 5, (composed of Dragon Skin 30 and Ecoflex 00-30 with 66.7% length portion) and a single material sensor stretched with an increment of 0.01 mm. (b) Sensor signals (digital bits) of the sensors stretched with an increment of 0.03 mm. (c) Sensor signal (resistance change) of a multi-material sensor designed with the material combination of Ecoflex 00-30 and an Ecoflex–DragonSkin mixture, and the 50% length portion, stretched up to 100% strain over 10000 cycles. (d) Tensile test result of the multi-material sensor with the highest sensitivity (66.7% length portion).

single-material sensors. The bell-shape proves that the multi-material sensors are superior in sensitivity to the single-material sensors, showing enhancement in sensitivity up to 33% and 9% for the two material combinations. Furthermore, the peaks in the curves in Fig. 5(c) suggests the existence of the optimal length portion. This observation extends the conclusions drawn in the mathematical analysis in Section 2.2.2 to include even general cases of soft sensors, confirmed through the actual prototypes composed of hyperelastic materials.

Overall, the observations on the distinct level of improvement in sensitivity between the two stiffness ratios and on the existence of the optimal length portion concur with the analysis in Section 2.2.2 and Fig. 3. However, for more sophisticated and accurate evaluation of the sensor model, the comparison of the experimental results with the theoretical predictions was elaborated through the hyperelastic force–strain relation in Section 3.2. The prediction is shown with the dotted line curve in Fig. 5(c), whose shape and relative location of the peak are in agreement with those of the experimental results. This result confirms that we can accurately predict the improvement in the sensitivity, given its length portion and the material properties (i.e. Yeoh coefficients).

4.2. Stiffness increase with stiffer materials or larger length portions: How to exploit both of sensitivity and softness?

Figs. 5(d), 5(e), and 5(f) illustrate the tensile forces measured during stretching and releasing of the sensors. It is apparent that increase in length portion leads to larger tensile forces, since the stiffer material occupies the major portion of the total structure. In addition, particularly in this experiment, larger tensile forces were observed in the sensors with high stiffness ratios in Fig. 5(d) than those with low stiffness ratios in Fig. 5(e). This is because the stiffer material (Dragon Skin 30) was used to create the larger stiffness ratio. However, increase in the stiffness ratio does not necessarily increase the overall stiffness. For example, using a material combination of Ecoflex–DragonSkin mixture and a material softer than Ecoflex 00-30 will have a higher stiffness ratio while showing a smaller overall stiffness compared to the sensors in Fig. 5(e). This means a sensitive yet soft sensor can be designed—an idea that will be discussed in detail in Section 6.

4.3. Higher resolution of multi-material sensor

Enhancement of the sensitivity due to the multi-material structure led to an increased resolution with a high signal-to-noise ratio. The multi-material sensor with the highest sensitivity, observed in Fig. 5(c), and a single-material sensor were stretched with increments of 0.01 mm and 0.03 mm, as shown in Fig. 6(a) and (b), respectively. The signals were obtained using a 16-bit analog-to-digital converter (ADS1115, Texas Instruments) with the maximum gain of 16. The results in Fig. 6(a) demonstrates that the multi-material sensor was able to clearly detect each 0.01 mm displacements while the signal changes of the single-material sensor was not distinguishable from the noise. The highest resolution of the single-material sensor was 0.03 mm in Fig. 6(b), significantly larger than that of the multi-material sensor. The practical advantage of such enhancement in sensitivity is highlighted in the following Section 5.

4.4. Hysteresis, linearity, dynamic durability, and the maximum strain of multi-material sensors

Multi-material sensors showed low hysteresis in Fig. 5(a). They also exhibited small and uniform nonlinearity (calculated with the error from the best fit line [41]), as described in Table 1, an attribute of their sensing mechanism (See Eq. (1)), independent of the stiffness ratio and the length portion. Furthermore, Fig. 6(c) shows the sensor signals of a multi-material sensor composed of Ecoflex–DragonSkin mixture and Ecoflex 00-30 with a 50% length portion during 10,000 stretching-releasing cycles with 100% strain. The consistent output signal proves that the multi-material design was highly durable under long-term dynamic loads. The results prove that the multi-material structure did not undermine the advantageous characteristics of the geometry-based fluidic sensors in terms of hysteresis, linearity, and dynamic durability. Fig. 6(d) shows the result of a tensile test of the multi-material sensor with the highest sensitivity in Fig. 5(c). The maximum measurable strain was 2.87, at which the sensor was fractured. A mechanical failure occurred at the interface between the stiff and soft materials, caused by large stress concentrations induced by the abrupt change in the cross-sectional area [42,43]. Potential improvements of the interface design to enhance the structural integrity and the measurable strain range of the multi-material sensors will be discussed in Section 6.2.

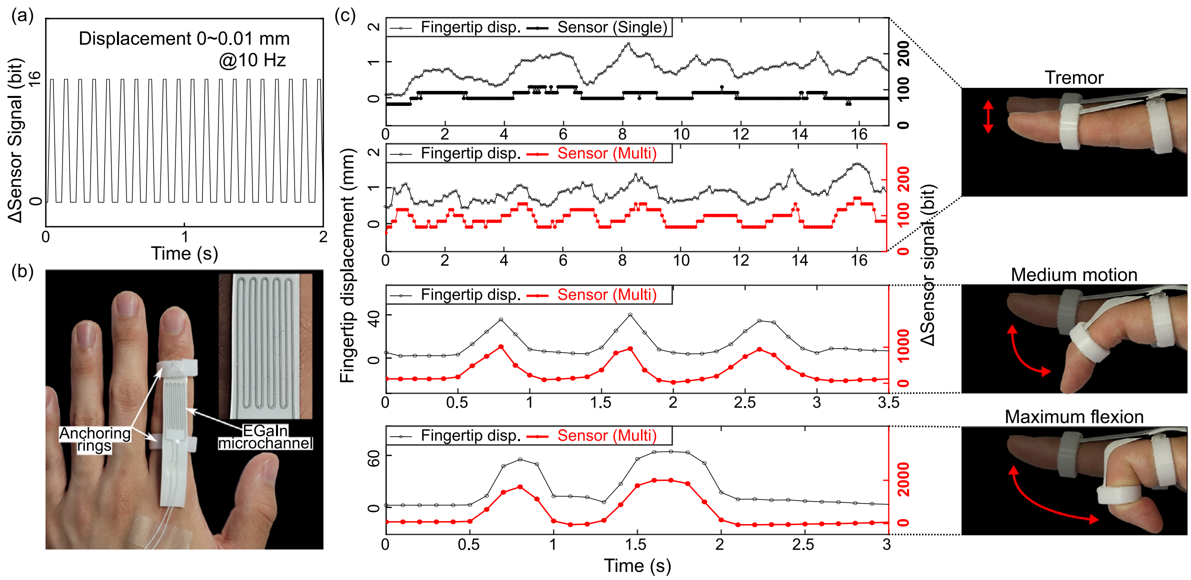

Fig. 7. Multi-material sensors for measuring finger movements. (a) Multi-material sensor signal (digital bit) subject to cyclic stretching and releasing of 0.01 mm displacement (its highest resolution) at 10 Hz. (b) Multi- or single-material sensor prototype mounted on the proximal interphalangeal joint. (c) Sensor signals obtained during various finger motions. From top to bottom: single material sensor readings (black) for fine finger motions similar to tremor, multi-material sensor readings (red) for flexion/extension motions from a small to the maximum ranges. (For interpretation of the references to color in this figure legend, the reader is referred to the web version of this article.)

5. Application

Involuntary finger motions, known as tremor, is present in all people. The average resting tremor of a young healthy individual (aged 20–30) is 0.1 mm ± 0.1 mm at frequencies lower than 10 Hz [29]. We demonstrate the ability of multi-material sensors to measure the wide range of finger motions with an exceptional precision that can even detect the tremor. The sensor is placed on the index proximal interphalangeal joint of a male human hand, and the strain caused by the rotation of the joint is measured. The distance from the joint to the fingertip and the radius of the joint were measured to be 49.1 mm and 7.6 mm, respectively. With these measurements, the displacement by the strain at the joint caused by the fingertip displacement of 0.1 mm was estimated as 0.015 mm, which was not detectable by the conventional single material sensor, as found in Fig. 6.

To verify that the sensor can perform reliably at the frequency of the tremor, a multi-material sensor that exhibited the highest sensitivity in Fig. 5(c) (composed of Dragon Skin 30 and Ecoflex 00-30 with a length portion of 66.7%) was subject to cyclic stretching and releasing with an amplitude 0.01 mm at a frequency of 10 Hz. The results, in Fig. 7(a), demonstrate that the multi-material sensor still maintains its highest resolution of 0.01 mm during high frequency motions, such as tremor.

The selected multi-material sensor and a single-material sensor were mounted on the joint, as depicted in Fig. 7(b). Their signals were recorded for the flexion and extension motions with the maximum and a slightly reduced ranges and also the fine finger motions that mimicked the tremor. The reference fingertip positions were also tracked by post-processing the recorded videos with a motion analysis software (ProAnalyst, Xcite). The results in Fig. 7(c) clearly demonstrate that the multi-material sensor signals (colored in red) successfully reflected the fingertip displacements as large as 58.4 mm and as small as 0.2 mm, whereas the single-material sensor failed to distinguish the small displacements.

6. Discussion

6.1. Design improvements for symmetry and conformity

Looking back at Fig. 2, it is noted that the asymmetric and non-uniform span of the stiffness of the component materials causes irregular deformation and abrupt changes in the cross-section when stretched. Asymmetric deformation hinders the conformity of the sensor to a large deformable surface, such as the joints in the human body, and sudden reduction in the cross-section induces stress concentration.

Fig. 8 shows the results of finite element analyses of various designs of multi-material sensors with (a) varied numbers of material interfaces, (b) additional material at the interface, (c) increased area of the interface, and (d) thickness variations. Despite the different designs, the overall strain plots show that the segments of the same material still experience uniform and equal strain levels. This approves that the assumptions behind Eqs. (3)–(7) can also be applied to the new designs. Using these findings, all the sensors in Figs. 8(a), 8(b), and 8(c) were designed to have constant sensitivities for a more objective assessment of their structural integrity.

The sensors in Fig. 8(a)-ii–iv shows symmetric and uniform deformations for better conformity to the host structure, while sharing the same stiffness ratio and the length portion with the sensor in Fig. 8(a)-i.

However, increasing the segmentation of the component material intensifies the stress concentration at the interfaces, marked in the stress contour plots. Fig. 8(a)-v graphs the stress concentration factor of each sensor, K_c, defined as

$$K_c = \frac{\sigma_{max}}{\sigma_{nom}}, \tag{11}$$

where the maximum stress (σ_{max}) occurs at the material interfaces and the nominal stress (σ_{nom}) is the average uniform stress [44]. Sensors with more material interfaces (Fig. 8(a)-ii–iv) generally show higher stress concentration factors at the interfaces. This may be critical to the sensor integrity, as shown in Fig. 6(d), where a mechanical failure was observed at the material interface, limiting the sensor's maximum strain.

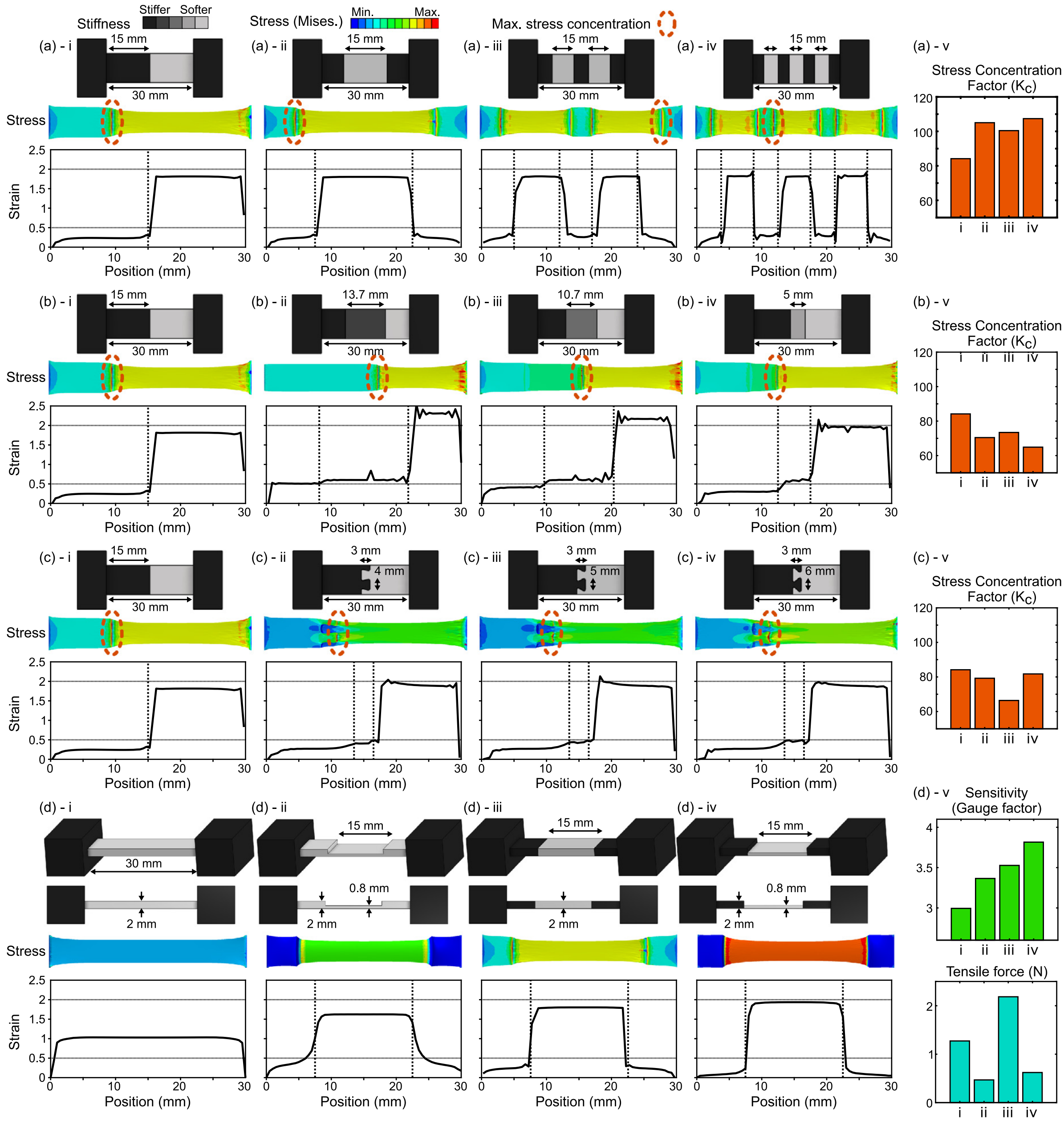

Fig. 8. Finite element analysis of various designs of multi-material sensors. The stress contours and the strain distributions at 100% strain are illustrated. For comparison of the stress concentration factors, all the sensors in (a)–(c) are designed to have the same sensitivity but with (a) varied numbers of material interfaces, (b) additional intermediate material segment whose stiffness is interpolated at the 1/6, 1/3, 1/2 point from the stiff to soft material for ii–iv, respectively, and (c) increased interfacial area from 1x to 1.8x using a jigsaw pattern. Sensitivities and tensile forces are compared between single- and multi-material sensors with thickness variations in (d).

6.2. Design improvements for structural integrity

The following two designs can alleviate stress concentration at the material interfaces. The simulation results of the first design are shown in Fig. 8(b), in which we introduce an additional material with an intermediate stiffness at the interface, as was done by Bartlett et al. [45]. The stiffness of the interfacial material was selected by linear interpolation of the Yeoh coefficients of Ecoflex 00-30 and Dragon Skin 30, at the 1/6 (ii), 1/3 (iii), and midpoint (iv) from Dragon Skin 30. For each case, the length of the material segments were adjusted to produce the same sensitivity. This gradation of the stiffness caused a more gradual distribution of stress along the length of the sensor, and decreased the stress concentration factor (Fig. 8(b)-v). The second design (Fig. 8(c)) was inspired by the work by Mengüç et al. [14], which increased the area of the material interface using a jigsaw geometry. We also observed a significant decrease in the stress concentration factor in sensors with a larger interface area than that of the original design (Fig. 8(c)-v). These enhancements at the material interface will allow multi-material sensors to endure larger strains before failures.

6.3. Design improvements for softness

The multi-material approach to enhancing sensitivity, as discussed in Section 4.2 with Fig. 5, may induce increase in overall stiffness when stiff materials are employed. Also, at the interface between the different materials, there are higher chances of mechanical failures due to the high stress concentration, as observed in Fig. 6(d) and Fig. 8(a)–(c). To Avoid these problems, using a single material but varying its thickness can be an alternative way to create the non-uniform strain distribution. As shown in Fig. 8(d)-i, ii and v, the segments with different thicknesses of the same material behave like distinct material segments. The thin segment works as a soft material while the thick segment works as a stiff material, demonstrating a higher sensitivity than the single-material sensor with a uniform thickness. Furthermore, combining the thickness variation with the multi-material structure, as shown in Fig. 8(d)-iv, may lead to even a higher sensitivity and also a drastically lower stiffness than a simple single- or multi-material sensor with a uniform thickness (Fig. 8(d)-i, iii).

7. Conclusion

The geometry-based sensing mechanism embedded with conductive fluid has its unique advantages: infinite stretchability of the conductive fluid, robust interface between the polymer and the conducting materials, and a reliable sensor performance based on the non-destructive nature. While enhancement in the sensitivities of geometry-based fluidic sensors has been known to be limited, this study presents a new approach to tackle the issue through non-uniform distribution of strain along the length of the sensor. The concept was realized by combining different materials with different stiffnesses. Taking the combination of Dragon Skin 30 and Ecoflex 00-30 as an example, we achieved the maximum gauge factor of 4, which is an increase in sensitivity by 33% compared to conventional single-material sensors.

The proposed multi-material sensors also demonstrated superb sensor performances in terms of resolution, hysteresis, linearity, and dynamic durability. Particularly, an enhanced resolution of 0.01 mm (0.0003 in strain) was achieved by the multi-material sensor, which enabled measurement of even tremors of the human hand. We also suggested design variations for improving symmetry, alleviating the stress concentration, and for reducing the stiffness, which can be uniquely combined to create highly sensitive but structurally robust sensors. Ultimately, through the analysis, the demonstration, and the suggested designs in this paper, it was confirmed that multi-material soft sensors have a high potential in various challenging systems in real-world applications.

Declaration of competing interest

The authors declare that they have no known competing financial interests or personal relationships that could have appeared to influence the work reported in this paper.

Data availability

Data will be made available on request.

Acknowledgments

This work was supported in part by the National Research Foundation, South Korea funded by the Korea Government (MSIT) [grant numbers 2016R1A5A1938472, 2021R1A2C2093790]; and in part by the Institute of Information & Communications Technology Planning & Evaluation (IITP) funded by the Korea Government (MSIT) [grant number 2021-0-00896].

References

[1] M. Amjadi, Y.J. Yoon, I. Park, Ultra-stretchable and skin-mountable strain sensors using carbon nanotubes–Ecoflex nanocomposites, Nanotechnology 26 (37) (2015) 375501.
[2] Y. Cheng, R. Wang, J. Sun, L. Gao, A stretchable and highly sensitive graphene-based fiber for sensing tensile strain, bending, and torsion, Adv. Mater. 27 (45) (2015) 7365–7371.
[3] A. Atalay, V. Sanchez, O. Atalay, D.M. Vogt, F. Haufe, R.J. Wood, C.J. Walsh, Batch fabrication of customizable silicone-textile composite capacitive strain sensors for human motion tracking, Adv. Mater. Technol. 2 (9) (2017) 1700136.
[4] M. Amjadi, K.U. Kyung, I. Park, M. Sitti, Stretchable, skin-mountable, and wearable strain sensors and their potential applications: A review, Adv. Funct. Mater. 26 (11) (2016) 1678–1698.
[5] S. Wu, S. Peng, Y. Yu, C.H. Wang, Strategies for designing stretchable strain sensors and conductors, Adv. Mater. Technol. 5 (2) (2020) 1900908.
[6] H. Souri, H. Banerjee, A. Jusufi, N. Radacsi, A.A. Stokes, I. Park, M. Sitti, M. Amjadi, Wearable and stretchable strain sensors: Materials, sensing mechanisms, and applications, Adv. Intell. Syst. 2 (8) (2020) 2000039.
[7] Y.L. Park, B.R. Chen, R.J. Wood, Design and fabrication of soft artificial skin using embedded microchannels and liquid conductors, IEEE Sens. J. 12 (8) (2012) 2711–2718.
[8] M.g. Kim, H. Alrowais, S. Pavlidis, O. Brand, Size-scalable and high-density liquid-metal-based soft electronic passive components and circuits using soft lithography, Adv. Funct. Mater. 27 (3) (2017) 1604466.
[9] D.Y. Choi, M.H. Kim, Y.S. Oh, S.H. Jung, J.H. Jung, H.J. Sung, H.W. Lee, H.M. Lee, Highly stretchable, hysteresis-free ionic liquid-based strain sensor for precise human motion monitoring, ACS Appl. Mater. Interfaces 9 (2) (2017) 1770–1780.
[10] W. Shan, T. Lu, C. Majidi, Soft-matter composites with electrically tunable elastic rigidity, Smart Mater. Struct. 22 (8) (2013) 085005.
[11] M.g. Kim, B. Lee, M. Li, S. Noda, C. Kim, J. Kim, W.J. Song, S.W. Lee, O. Brand, All-soft supercapacitors based on liquid metal electrodes with integrated functionalized carbon nanotubes, ACS Nano 14 (5) (2020) 5659–5667.
[12] T.T. Hoang, J.J.S. Quek, M.T. Thai, P.T. Phan, N.H. Lovell, T.N. Do, Soft robotic fabric gripper with gecko adhesion and variable stiffness, Sensors Actuators A 323 (2021) 112673.
[13] M.g. Kim, H. Alrowais, O. Brand, 3D-integrated and multifunctional all-soft physical microsystems based on liquid metal for electronic skin applications, Adv. Electron. Mater. 4 (2) (2018) 1700434.
[14] Y. Mengüç, Y.L. Park, H. Pei, D. Vogt, P.M. Aubin, E. Winchell, L. Fluke, L. Stirling, R.J. Wood, C.J. Walsh, Wearable soft sensing suit for human gait measurement, Int. J. Robot. Res. 33 (14) (2014) 1748–1764.
[15] Y. Yoon, S. Kim, D. Kim, S.K. Kauh, J. Lee, Four degrees-of-freedom direct writing of liquid metal patterns on uneven surfaces, Adv. Mater. Technol. 4 (2) (2019) 1800379.
[16] S. Kim, J. Oh, D. Jeong, J. Bae, Direct wiring of eutectic gallium–indium to a metal electrode for soft sensor systems, ACS Appl. Mater. Interfaces 11 (22) (2019) 20557–20565.
[17] W. Dong, Y. Wang, Y. Zhou, Y. Bai, Z. Ju, J. Guo, G. Gu, K. Bai, G. Ouyang, S. Chen, et al., Soft human–machine interfaces: Design, sensing and stimulation, Int. J. Intell. Robot. Appl. 2 (3) (2018) 313–338.
[18] T. Kim, S.J. Yoon, Y.L. Park, Soft inflatable sensing modules for safe and interactive robots, IEEE Robot. Autom. Lett. 3 (4) (2018) 3216–3223.
[19] H. Wang, M. Totaro, L. Beccai, Toward perceptive soft robots: Progress and challenges, Adv. Sci. 5 (9) (2018) 1800541.
[20] J. Morrow, H.S. Shin, C. Phillips-Grafflin, S.H. Jang, J. Torrey, R. Larkins, S. Dang, Y.L. Park, D. Berenson, Improving soft pneumatic actuator fingers through integration of soft sensors, position and force control, and rigid fingernails, in: 2016 IEEE International Conference on Robotics and Automation, ICRA, IEEE, 2016, pp. 5024–5031.
[21] V. Wall, G. Zöller, O. Brock, A method for sensorizing soft actuators and its application to the rbo hand 2, in: 2017 IEEE International Conference on Robotics and Automation, ICRA, IEEE, 2017, pp. 4965–4970.
[22] L.Y. Zhou, Q. Gao, J.F. Zhan, C.Q. Xie, J.Z. Fu, Y. He, Three-dimensional printed wearable sensors with liquid metals for detecting the pose of snakelike soft robots, ACS Appl. Mater. Interfaces 10 (27) (2018) 23208–23217.
[23] T.T. Hoang, P.T. Phan, M.T. Thai, N.H. Lovell, T.N. Do, Bio-inspired conformable and helical soft fabric gripper with variable stiffness and touch sensing, Adv. Mater. Technol. 5 (12) (2020) 2000724.
[24] L.R. Volpatti, A.K. Yetisen, Commercialization of microfluidic devices, Trends. Biotechnol. 32 (7) (2014) 347–350.
[25] T.N. Do, Y. Visell, Stretchable, twisted conductive microtubules for wearable computing, robotics, electronics, and healthcare, Sci. Rep. 7 (1) (2017) 1–12.
[26] F. Weichert, D. Bachmann, B. Rudak, D. Fisseler, Analysis of the accuracy and robustness of the leap motion controller, Sensors 13 (5) (2013) 6380–6393.

[27] C. Mizera, T. Delrieu, V. Weistroffer, C. Andriot, A. Decatoire, J.P. Gazeau, Evaluation of hand-tracking systems in teleoperation and virtual dexterous manipulation, IEEE Sens. J. 20 (3) (2019) 1642–1655.

[28] P.R. Burkhard, J.W. Langston, J.W. Tetrud, Voluntarily simulated tremor in normal subjects, Neurophysiol. Clin. Clin. Neurophysiol. 32 (2) (2002) 119–126.

[29] M.M. Sturman, D.E. Vaillancourt, D.M. Corcos, Effects of aging on the regularity of physiological tremor, J. Neurophysiol. 93 (6) (2005) 3064–3074.

[30] J.C. Case, E.L. White, R.K. Kramer, Soft material characterization for robotic applications, Soft Robot. 2 (2) (2015) 80–87.

[31] E.L. White, J.C. Case, R.K. Kramer, Multi-mode strain and curvature sensors for soft robotic applications, Sensors Actuators A 253 (2017) 188–197.

[32] M. Park, Y. Ohm, D. Kim, Y.L. Park, Multi-material soft strain sensors with high gauge factors for proprioceptive sensing of soft bending actuators, in: 2019 2nd IEEE International Conference on Soft Robotics, RoboSoft, IEEE, 2019, pp. 384–390.

[33] H.J. Kim, C. Son, B. Ziaie, A multiaxial stretchable interconnect using liquid-alloy-filled elastomeric microchannels, Appl. Phys. Lett. 92 (1) (2008) 011904.

[34] Y.L. Park, C. Majidi, R. Kramer, P. Bérard, R.J. Wood, Hyperelastic pressure sensing with a liquid-embedded elastomer, J. Micromech. Microeng. 20 (12) (2010) 125029.

[35] T.V. Neumann, M.D. Dickey, Liquid metal direct write and 3D printing: A review, Adv. Mater. Technol. 5 (9) (2020) 2000070.

[36] G. Shin, B. Jeon, Y.L. Park, Direct printing of sub-30 μm liquid metal patterns on three-dimensional surfaces for stretchable electronics, J. Micromech. Microeng. 30 (3) (2020) 034001.

[37] L. Mullins, Softening of rubber by deformation, Rubber Chem. Technol. 42 (1) (1969) 339–362.

[38] J. Diani, B. Fayolle, P. Gilormini, A review on the mullins effect, Eur. Polym. J. 45 (3) (2009) 601–612.

[39] P.L.S. Martins, R.M. Natal Jorge, A.J.M. Ferreira, A comparative study of several material models for prediction of hyperelastic properties: Application to silicone-rubber and soft tissues, Strain 42 (3) (2006) 135–147.

[40] M. Shahzad, A. Kamran, M.Z. Siddiqui, M. Farhan, Mechanical characterization and FE modelling of a hyperelastic material, Mater. Res. 18 (2015) 918–924.

[41] S. Din, W. Xu, L.K. Cheng, S. Dirven, A stretchable multimodal sensor for soft robotic applications, IEEE Sens. J. 17 (17) (2017) 5678–5686.

[42] M. Tatari, A. Mohammadi Nasab, K.T. Turner, W. Shan, Dynamically tunable dry adhesion via subsurface stiffness modulation, Adv. Mater. Interfaces 5 (18) (2018) 1800321.

[43] A. Luo, A.M. Nasab, M. Tatari, S. Chen, W. Shan, K.T. Turner, Adhesion of flat-ended pillars with non-circular contacts, Soft Matter 16 (41) (2020) 9534–9542.

[44] R. Brighenti, A. Spagnoli, A. Carpinteri, F. Artoni, Notch effect in highly deformable material sheets, Thin-Walled Struct. 105 (2016) 90–100.

[45] N.W. Bartlett, M.T. Tolley, J.T.B. Overvelde, J.C. Weaver, B. Mosadegh, K. Bertoldi, G.M. Whitesides, R.J. Wood, A 3D-printed, functionally graded soft robot powered by combustion, Science 349 (6244) (2015) 161–165.